

Imaging Endogenous Bilirubins with Two-Photon Fluorescence of Bilirubin Dimers

Yu-Fang Shen,^{†,||} Ming-Rung Tsai,^{†,‡} Shao-Chieh Chen,[†] Yun-Shiuan Leung,[‡] Chien-Tai Hsieh,[†] Yu-Shing Chen,[†] Fu-Lien Huang,[†] Rofeamor P. Obena,[⊥] Medel Manuel L. Zulueta,[#] Hsin-Yi Huang,[∇] Wen-Jeng Lee,[○] Kuo-Chun Tang,[‡] Chun-Ta Kung,[§] Min-Huey Chen,^{||} Dar-Bin Shieh,[◆] Yu-Ju Chen,[⊥] Tzu-Ming Liu,^{*,†} Pi-Tai Chou,^{*,‡} and Chi-Kuang Sun^{*,§}

[†]Institute of Biomedical Engineering, [‡]Department of Chemistry, and [§]Graduate Institute of Photonics and Optoelectronics, National Taiwan University, Taipei 10617, Taiwan

^{||}3D Printing Medical Research Center, China Medical University Hospital, Taichung City 40447, Taiwan

[⊥]Institute of Chemistry, and [#]Genomics Research Center, Academia Sinica, Taipei 11529, Taiwan

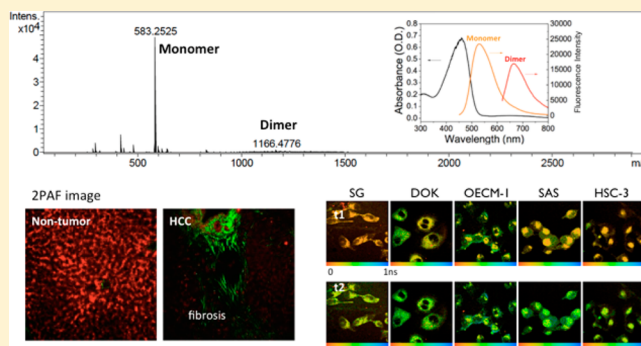
[∇]Department of Pathology, and [○]Department of Medical Imaging, National Taiwan University Hospital, Taipei 10051, Taiwan

[◆]Institute of Oral Medicine, National Cheng-Kung University, Tainan 70101, Taiwan

^{||}Graduate Institute of Clinical Dentistry, School of Dentistry, National Taiwan University, Taipei 10051, Taiwan

Supporting Information

ABSTRACT: On the basis of an infrared femtosecond Cr:forsterite laser, we developed a semiquantitative method to analyze the microscopic distribution of bilirubins. Using 1230 nm femtosecond pulses, we selectively excited the two-photon red fluorescence of bilirubin dimers around 660 nm. Autofluorescences from other endogenous fluorophores were greatly suppressed. Using this distinct fluorescence measure, we found that poorly differentiated hepatocellular carcinoma (HCC) tissues on average showed 3.7 times lower concentration of bilirubins than the corresponding nontumor parts. The corresponding fluorescence lifetime measurements indicated that HCC tissues exhibited a longer lifetime (500 ps) than that of nontumor parts (300 ps). Similarly, oral cancer cell lines had longer lifetimes (>330 ps) than those of nontumor ones (250 ps). We anticipate the developed methods of bilirubin molecular imaging to be useful in diagnosing cancers or studying the dynamics of bilirubin metabolisms in live cells.



Although commonly regarded as the waste product of heme catabolism, bilirubin has progressively become known for its versatile physiological functions during the past 2 decades. Bilirubin levels are most often elevated in patients with liver diseases or a blockage to bile flow, which can be measured by blood tests.^{1,2} Besides, bilirubin is a powerful antioxidant³ and anti-inflammatory agent⁴ that can assist the protection of lipids and prevent other kinds of oxidation.^{5,6} It also serves as one of the defense mechanisms in the serum against oxidative stress^{7,8} and may play a protective role for the cerebral,⁹ pulmonary,¹⁰ hepatobiliary,¹¹ cardiovascular, and immunological systems.^{5,12} Recently, several researches reported that serum bilirubin concentrations have negative correlations with cardiovascular diseases,^{4,13–16} arterial hypertension,¹⁷ diabetes mellitus,^{18,19} metabolic syndrome, and obesity.^{20–24} These clinical diagnosis indicate that bilirubin is a critical factor related to the progression or aggression of many diseases. To advance the diagnosis and treatment of these diseases, an imaging method to map the distribution of bilirubins is necessary.

Numerous approaches have been developed for the detection and quantitation of bilirubin in the past few years,^{25–42} among which direct spectroscopic measurement²⁵ and the diazo reaction²⁶ are the most common ones. However, these methods cannot be applied to time-course in vitro or in vivo studies, which are important for the advanced understanding of bilirubin metabolism in complex microenvironments of organisms. Therefore, a specific and sensitive contrast for bilirubin molecular imaging is required.

Bilirubin is a yellow-red pigment which has a strong absorption band around 440 nm⁴³ and an emission band at about 540–550 nm.⁴⁴ When it bound to human serum albumin (HSA), its fluorescence yield is increased and its emission maximum occurs at 534 ± 3 nm with maximum excitation at 462 ± 3 nm.⁴⁵ However, single-photon excitation at 400–500

Received: January 19, 2015

Accepted: July 6, 2015

Published: July 6, 2015

nm may also simultaneously excite other endogenous fluorophores such as flavins ($\lambda = 530$ nm), which overlap the fluorescence band of bilirubins. Recently, we found liver, a bilirubin-rich organ, has a 660 nm two-photon autofluorescence (2PAF) excited at 1230 nm (Figure 1).⁴⁶ Far away from two-

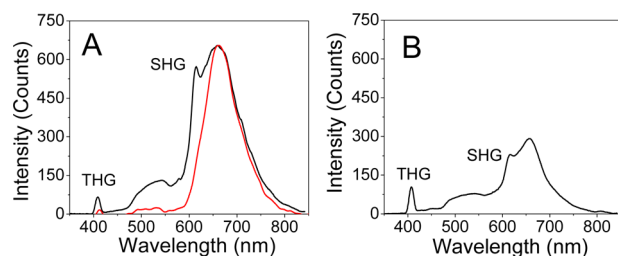


Figure 1. Multiphoton autofluorescence spectra of (A) nontumor liver and (B) poorly differentiated HCC liver under the excitation of femtosecond Cr:forsterite lasers. Red curve in panel A is the multiphoton fluorescence spectrum of bilirubin diglucuronide with its peak intensity equivalent with that of a nontumor one.

photon excitation of Soret bands, most of endogenous fluorophores will not be excited under this excitation condition. The possible candidates were limited to porphyrins, biliverdins, or bilirubins.⁴⁶ Through the fluorescence spectrum and lifetime measurement on standard chemicals, obviously, porphyrins (Supporting Information Figure S1) are quite different from those measured in liver tissues (Figure 1). The emission peaks of HSA-associated biliverdins are both at 690–700 nm under single-photon and multiphoton excitation (Supporting Information Figure S2, parts A and B), which is close to the 660 nm emission peak (Figure 1). However, their 2.3 ns fluorescence lifetime (Supporting Information Figure S2C) is much longer than the 100–400 ps 2PAF lifetimes observed in fresh liver tissues.⁴⁶ These results indicate that biliverdin and porphyrin have relatively rather small contribution on this red autofluorescence. Therefore, we thought this characteristic red fluorescence might be related to bilirubins and/or their derivatives and have potential to be a useful contrast for bilirubin molecular imaging.

In this study, using liquid chromatography–mass spectrometry (LC–MS) and fluorescence spectroscopy, we found that the red autofluorescence most likely originates from the bilirubin dimers. The 660 nm fluorescence spectral profiles and the fluorescence lifetimes are both similar to those acquired in living cells and liver tissues. When bilirubins are associated with HSA, we further found the three-photon fluorescence (3PF) of bilirubin monomer around 530 nm. Utilizing this distinct red fluorescence from dimers, we discovered that the poorly differentiated hepatocellular carcinoma (HCC) tissues on average show 3.7 times lower concentration of dimeric bilirubins than the corresponding nontumor parts. When the fluorescence lifetime of bilirubin dimers were measured, the HCC tissues showed a longer lifetime ($t_1 = 500$ ps) than the nontumor parts ($t_1 = 300$ ps). The oral cancer cells ($t_1 > 330$ ps) and the normal ones ($t_1 = 250$ ps) can also be differentiated by the lifetime measures. We anticipate such combinational approach, which contains fluorescence spectroscopy, microscopic distribution, and lifetime imaging, can be an efficient and direct tool for fast, sensitive, and accurate determination in diagnosing cancers or studying the dynamics of bilirubin metabolisms in live cells.

MATERIALS AND METHODS

Preparation of Bilirubin and Biliverdin Solutions.

Bilirubin hydrochloride and biliverdin hydrochloride were purchased from Sigma-Aldrich, U.S.A. An amount of 10 mg of bilirubin hydrochloride was dissolved in 0.05 M NaOH solution, and the solution was adjusted the pH to 7.4 with concentrated HCl. The final volume was made up with double distilled water (ddH_2O), and the final concentration of bilirubin solution was 1 mM. To have a better solubility of bilirubins, the 1 mM bilirubin solution was then added to the same volume of human serum albumin solution to form the 500 μM bilirubin–HSA solution. The preparation of 1 mM biliverdin and biliverdin–HSA solution followed the same procedures.

Liver Sections and Bile. All the liver cryosections were obtained from the tissue bank of the Center of Genomic Medicine, National Taiwan University. The residual bile was obtained from the patients with biliary drainage. The study on human HCC sections and the residual bile have been certified by the Research Ethics Committee of National Taiwan University Hospital (NTUH) with case number 200901006R. To ensure the freshness of liver sections, the liver tissues were embedded in optimal cutting temperature (OCT) medium right after surgery, preserved in -80 °C, and cryosectioned right before the imaging. The liver sections were taken from residual tissues of 19 HCC patients. For each patient, both tumor and nontumor parts of liver tissues were used for the experiments. The 30 μm thick sections were placed on the slide and covered with a coverglass. The slides were mounted on the microscope for the observation using multiphoton nonlinear optical microscopy and fluorescence lifetime imaging microscopy. All the measurements were done within an hour to reduce necrosis or apoptosis effects on hepatocytes. We also took 5 μm following sections cut from 30 μm sections for further pathological examinations or bile stains.

Pathological Examination on HCC Tissues. The pathological diagnoses of the sections were provided by the tissue bank based on the reports from the Department of Pathology, NTUH. To avoid local variation of tissues, the hematoxylin and eosin (H&E) staining on the adjacent 5 μm sections were used. The corresponding pathological status of liver sections was read by a certificated pathologist.

Bile Stain. For the bile stain, Fouchet's reagent was used to oxidize the bilirubin into green biliverdin.²⁸ Bile stain color may range from olive green to emerald green depending on the concentration of bile pigment presented. Staining solutions, Fouchet's reagent and Van Gieson's solutions, were freshly prepared prior to staining. Fouchet's reagent was prepared by mixing 12.5 g of trichloroacetic acid with 50 mL of ddH_2O and adding 5 mL of 10% ferric chloride. The Van Gieson's solution was prepared by mixing 1 mL of 1% acid fuchsin and 45 mL of saturated picric acid. The 5 μm adjacent sections were fixed by 10% formalin and then soaked in Fouchet's reagent for 5 min. After washing and rinsing by ddH_2O , the sections were soaked again in Van Gieson's solution for another 5 min. Finally, the sections were dehydrated and mounted.

Normal Oral Keratinocytes and Oral Cancer Cells. The normal SG cell was obtained from Dr. Min-Huey Chen (National Taiwan University, Taiwan), DOK, OECM-1, SAS, and HSC-3 cells were obtained from Dr. Dar-Bin Shieh (National Cheng Kung University, Taiwan). SG and SAS were cultured in Dulbecco's modified Eagle's medium (DMEM). DOK cells were cultured in DMEM with 5 $\mu\text{g}/\text{mL}$ hydro-

cortisone. OECM-1 cell line was established from primary tumors of adult male OSCC patients (Taiwan) with a history of betel quid chewing^{47,48} and was grown in Roswell Park Memorial Institute (RPMI) 1640 medium. HSC-3 derived from human tongue carcinoma with lymph node metastasis was obtained from the Japanese Collection of Research Bioresources Cell Bank of Japan and was grown in minimum essential medium (MEM). All culture mediums were added with 10% fetal bovine serum, 2 mmol/L L-glutamine, and antibiotics. Cells were maintained at 37 °C and 5% CO₂.

Characterizing Single-Photon Properties of Bilirubin and Biliverdin Solutions. The single-photon properties of bilirubin and biliverdin solutions were measured by an absorption spectrometer (Hitachi, U-3310) and a fluorescence spectrometer (Edinburgh, FS920). All the bilirubin and biliverdin solutions were filled in cuvettes for measurements.

Multiphoton Nonlinear Microscopy and Fluorescence Lifetime Imaging Microscopy System. The imaging instrument for multiphoton nonlinear microscopy is composed of a home-built femtosecond Cr:forsterite laser, a scanning unit (FV300, Olympus), an inverted optical microscope, a 2D translation stage, three photomultiplier tubes (PMTs), and an image acquisition software. The femtosecond Cr:forsterite laser is operating around 1230 nm with a pulse width of 100 fs. The typical output power is 400 mW. The laser beam was scanned by galvanometer mirrors and passed through the 865 nm edged dichroic beam splitter (Chroma). Then the scanned laser beam was focused by a water immersion objective (20× NA = 0.95) onto liver sections for the generation of nonlinear optical signals. To avoid the saturation of two-photon autofluorescences, the power was kept below 80 mW after the objective. In our study, the optical contrasts of the multiphoton nonlinear microscopy include the second-harmonic generation (SHG), the 2PAF, and the third-harmonic generation (THG) of liver sections. The point-by-point generated signals were reflected by dichroic beam splitter and detected by PMTs. The 512 × 512 pixels images (720 μm × 720 μm field of view) were reconstructed by the imaging acquisition program. The in vivo sectioning capability and the submicrometer spatial resolution of this developed system have been demonstrated and described elsewhere.^{49–51}

To measure the spectra of multiphoton signals, we used a thermoelectrically cooled charge-coupled device (CCD) spectrometer. The temperature was cooled down to -60 °C for higher signal-to-noise ratio. The multiphoton signals generated from liver sections or chemical solutions were reflected by an 865 nm edged dichroic beam splitter and then focused onto the slit of the spectrometer by a lens with 10 cm focal distance. The open width of the slit is 200 μm, and the integration time is 10 s for all spectral measurements. All the spectra were calibrated by a Hg (Ne) lamp.

For fluorescence lifetime measurement, a time-correlated single-photon counting (TCSPC) system (Becker and Hickl; SPC-830) adapted to an inverted optical microscope was employed. The objective used for fluorescence lifetime measurement was another 60× NA = 0.9 water immersion objective. We used a photon counting PMT with ~160 ps width of instrument response function (IRF). The single-photon arriving time relative to the excitation pulses was counted and recorded. The trace of fluorescence decay can then be represented by a histogram of photon arriving times. Using a multiexponential decay model and a deconvolution with IRF, the extracted fluorescence lifetime can be shorter than 160 ps

with $\sim \pm 60$ ps standard deviation. To reduce the interference and avoid the dominance from second-harmonic generation signals, we used a 625 nm long pass filter to block SHG (~615 nm). Since the pulse repetition period of our Cr:forsterite laser is ~10 ns, we can observe the lifetime of red autofluorescences no longer than 10 ns. Therefore, the presence of red-fluorescent porphyrins with typical ~16 ns lifetime⁵² will cause an elevation of dc level in our measurement (see Supporting Information Figure S1B). In our experiments, such kind of dc background signals were small compared with those from bilirubins, indicating that the concentration of free porphyrins is quite small in hepatocytes. By a synchronization with the scanning unit, the fitted lifetime of each pixel resulted in a 256 × 256 pixels (120 μm × 120 μm field of view) microscopic image of fluorescence lifetime. The image integration time for each image was ~10 min, which was set for good enough signal-to-noise ratio.

Regarding the curve fitting of fluorescence lifetimes, we used the strong second-harmonic generation signals generated from silicon nanoparticles⁵³ to obtain the IRF. This calculated IRF was applied to deconvolute all traces we measured including the fluorescence-lifetime imaging microscopy (FLIM) data. Using IRF and a two-exponential decay model, the fitting software calculated the lifetimes [t₁, t₂] and their weighting percentages of amplitudes [a₁, a₂]. The fitting was best achieved by minimizing the error χ^2 values close to 1.

The histogram of fluorescence lifetimes were created according to the image area we selected. For the lifetime histogram of bright granules that appeared in cells, pixels in bright granules were selected. By excluding pixels in those bright granules, other pixels within cells will result in a lifetime histogram of cytoplasm.

Statistical Analysis. We used two-sample paired *t* test statistics to check whether the average 2PAF pixel counts of nontumor liver sections were significantly larger than those of poorly differentiated HCC. The significant level we used is *p* < 0.05.

LC–MS Analysis. Samples were analyzed by LC–MS on an Agilent 1260 HPLC system (Waldbronn, Germany) coupled with a Bruker micrOTOF-Q II mass spectrometer (Billerica, MA). Each sample was loaded onto a 4.6 mm × 100 mm Agilent Zorbax Eclipse Plus C18 column and separated at a flow rate of 0.8 mL/min using a linear gradient of 5–70% acetonitrile in water for 30 min, and held at 70% for an additional 5 min. Electrospray ionization condition: N₂ for nebulization (0.8 bar) and drying (flow of 6.0 L/min, temperature of 180 °C), and the capillary voltage was 4500 V. Each mass scan (50–3000 *m/z*) was acquired at a resolution of 17 500 fwhm (at 922 *m/z*).

RESULTS AND DISCUSSION

Characterizing the Fluorescence Spectra and Lifetimes of the Bilirubins. Using standard bilirubin powders, solution of bilirubin associated with HSA had a peak absorption around 460 nm (Figure 2, black curve). When excited at this wavelength, the fluorescence spectrum had a 530 nm emission peak (Figure 2, orange curve). When we excited the bilirubins at 615 nm, we found another unexpected 660 nm emission peak (Figure 2, red curve). The fluorescence excitation spectrum measured at 660 nm emission showed a maximal yield around 600 nm (Supporting Information Figure S3), indicating there were other chemical species mixed in solutions. In order to study the origin of the red fluorescence, we then

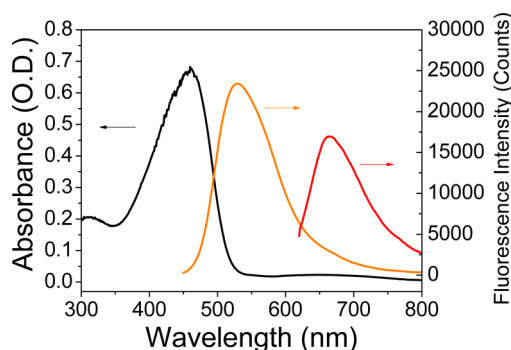
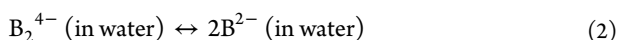


Figure 2. Absorption spectra (black curve), 430 nm excited emission spectra (orange curve), and 615 nm excited emission spectra (red curve) of bilirubins associated with human serum albumin.

performed LC–MS analyses on bilirubin solutions with and without HSA at pH 7.4. Both solutions revealed MS signals at the doubled molecular weight (Supporting Information Figure S4), indicating the presence of dimers. According to literatures, the diacid bilirubin BH_2 can dissociate into protons and the dianion B^{2-} in alkaline solutions (see eq 1).⁵⁴ Two dianions of bilirubin can further form bilirubin dimers B_2^{4-} (see eq 2).^{55–57}



One of the possible dimer structures is ascribed to a hydrogen-bonding dimer, in which the quadruple intermolecular hydrogen bonds form between pyromethenone and pyromethenone of two bilirubin molecules.⁵⁸ If the red fluorescence originated from bilirubin dimers, then higher pH value should result in stronger fluorescence intensities. To study the pH dependence of 660 nm fluorescence, we used bilirubin powders dissolved in NaOH solutions and titrated by HCl to different pH values (pH 7.4, pH 9, and pH 12). As we expected, the 615 nm excited 660 nm fluorescence was greatly enhanced at higher pH values (Figure 3A). As a negative control, the red fluorescence disappeared when the bilirubins were dissolved in DMSO (Figure 3A, red curve), in which the bilirubins were monomeric.⁵⁹ These evidence support that the bilirubin red fluorescence originates from its dimers. Although the single-photon fluorescence of bilirubin dimers was weak at pH 7.4 (Figure 3A, black curve), the intensity was enhanced 3 times after association with HSA (Figure 3B). This fluorescence enhancement might be due to a translational or vibrational immobilization of bilirubin dimers by HSA.⁶⁰

On the other hand, the excitation with 1230 nm femtosecond lasers also generates 660 nm two-photon fluorescence (2PF) in pH 7.4 bilirubin solutions (Figure 3, parts C and D). When the bilirubin is associated with HSA, an extra 530 nm 3PF peak can be found in the spectrum. This double-peak feature agreed well with what we observed in liver sections (Figure 1A). From both fluorescence spectra analysis and the LC–MS results we thought that the 530 nm three-photon autofluorescence (3PAF) peak originated from bilirubin monomers while the 2PAF peak most probably originated from bilirubin dimers.

In order to use these fluorescence contrasts as semi-quantitative measures on the concentration of bilirubins, we studied the concentration dependency under single-photon and multiphoton excitation. According to eqs 1 and 2, if more bilirubins BH_2 dissolved, concentrations of bilirubin dianions B^{2-} and dimers B_2^{4-} will be proportionally and quadratically

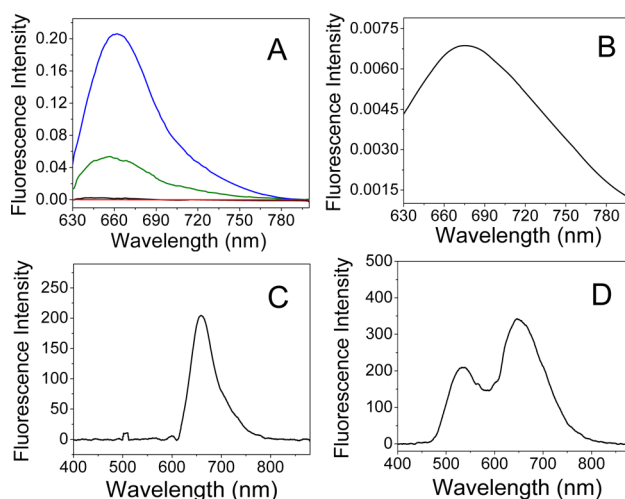


Figure 3. Fluorescence spectra of bilirubins. (A) The single-photon fluorescence spectrum of bilirubin solutions at pH 7.4 (black curve), pH 9 (green curve), pH 12 (blue curve), and dissolved in DMSO (red curve) without HSA. (B) The single-photon autofluorescence spectrum of bilirubin with HSA at pH 7.4. (C) The 2PF spectrum of bilirubin without HSA at pH 7.4. (D) The 2PF spectrum of bilirubin with HSA at pH 7.4. Note that an extra 530 nm 3PF peak was found.

increased, respectively. However, the protons from BH_2 will decrease the pH value of solutions and reduce the dissociation constant of BH_2 .^{54,55} Therefore, the formation of bilirubin dimers will be affected by the pH values of solutions and the dimer concentrations may not be quadratic-dependent on the concentration of BH_2 . As a result, the single-photon fluorescence intensities showed a linear dependence on BH_2 concentrations at pH 7.4 (Supporting Information Figure S5). Under multiphoton excitation at 1230 nm, both 2PF and 3PF intensities have nearly linear dependence on the bilirubin concentrations at pH 7.4 (Supporting Information Figure S6). These results indicate the red fluorescence of bilirubin dimers could serve as a useful imaging contrast to quantify the bilirubin dimers, and thus bilirubins. To reduce the potential interference from porphyrins and biliverdins, the suggested detection window is 650–670 nm.

We then characterized the 2PF lifetime of the bilirubin dimers. Under the multiphoton excitation with our 1230 nm femtosecond Cr:forsterite laser, the 1 mM bilirubins in buffer emitted red fluorescence around 666 nm with a full width at half-maximum (fwhm) of ~ 70 nm (Figure 4A, dashed black curve), and an emission peak around 410 nm was corresponding to the THG generated from the glass–solution interface. The very short lifetime (~ 125 ps) of bilirubin dimers in buffer solution (Figure 4B, dashed black curve) indicates that aggregation might have occurred because bilirubin is not hydrophilic and thus tends to aggregate in the aqueous medium. For 0.5 mM bilirubins associated with HSA (Figure 4A, solid black curve), the emission bandwidth is apparently narrower (fwhm ~ 42 nm) than that of the free bilirubins in buffer solution. The corresponding fluorescence reveals two components of exponential decay, consisting of a 240 ps ($a_1 = 60\%$) and a longer 1.2 ns components (Figure 4B, solid black curve). The longer component disappeared for the concentration smaller than 100 μM (Figure 4C). The water-soluble bilirubin diglucuronide isolated from human bile showed an

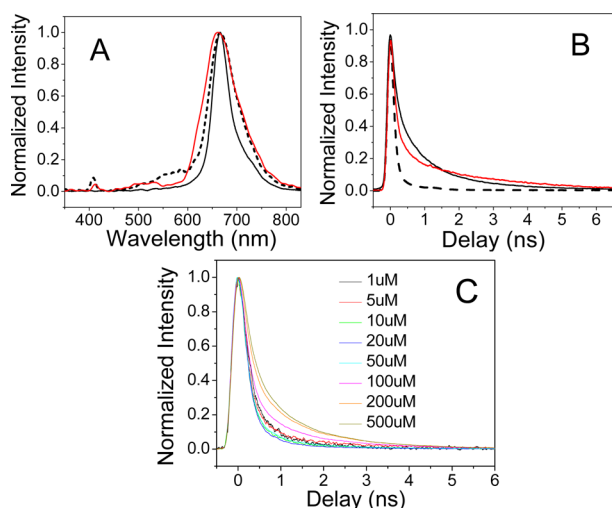


Figure 4. (A) Multiphoton spectra and (B) corresponding fluorescence lifetime traces of free bilirubins in buffer solution (dashed black curve), bilirubins associate with HSA (solid black curve), and bilirubin diglucuronides (solid red curve). (C) The 2PF lifetime of HSA-associated bilirubin at different concentrations from 1 to 500 μM .

emission peak around 662 nm with much broader bandwidth (fwhm ~ 83 nm, Figure 4A, solid red curve).

Interestingly, the 2PAF intensity of 2 μM bilirubin diglucuronides (conjugate bilirubins) is comparable to that generated from 0.5 mM unconjugated bilirubins, indicating much better emission efficiencies of the dimers of conjugated bilirubins. The dominant fluorescence lifetime of human bile was shortened to 140 ps ($a_1 = 85\%$) with a 2.34 ns longer component (Figure 4B, solid red curve). Obviously, either bilirubins or their catabolites (bilirubin diglucuronides) have sufficiently shorter 2PAF lifetimes than those of porphyrins and biliverdins.

Investigating the Molecular Origin of Red Autofluorescences in Hepatocytes. In order to confirm whether the red autofluorescences we found in liver section⁴⁶ came from bilirubin dimers, we measured the 2PAF microscopy in liver sections and compare the results with bile stain. With an 1230 nm femtosecond Cr:forsterite laser, the multiphoton fluorescence of most endogenous fluorophores like NADH, flavins, and bilirubins should be greatly suppressed. Only red-fluorescent fluorophores like porphyrins^{17,18} and biliverdins¹¹ could be efficiently excited. However, in the nontumor part of liver tissues, we typically observed strong red 2PAF around 660 nm accompanied by a yellow shoulder of 3PAF (Figure 1A, solid black curve). Obviously, 3PAF is the characteristic 530 nm emission of the bilirubin monomer (Figure 2, orange curve). As we described in the previous section, this unexpected 660 nm peak wavelength is quite different from those of porphyrins and biliverdins. Consequently, 2PAF of the tissue most likely originated from the dimers of bilirubins (Figure 4A, solid curves). The SHG and THG peaks in Figure 1 were contributed from collagens and lipid vesicles¹⁹ in tissues, respectively. Under the same excitation condition, the multiphoton autofluorescence spectrum of poorly differentiated HCC hepatocytes (Figure 1B) has a reduced intensity. To make sure if this reduction of 2PAF originates from the absence of bilirubins in HCC tissues, we performed a bile stain specific to the bilirubin molecules. As shown in Figure 5, parts A and B,

more bilirubins were present in the nontumor part (olive green color) than those in HCC regions (paler color).

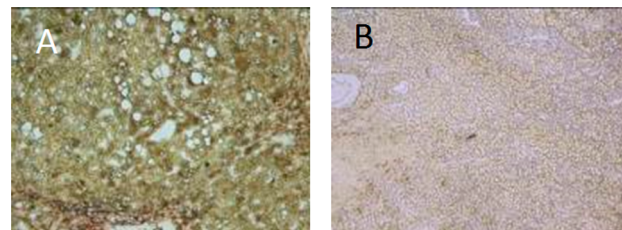


Figure 5. Bile stains of liver sections in (A) nontumor and (B) poorly differentiated HCC regions from the same patient.

To gain more morphological evidence, we then performed multiphoton nonlinear microscopy on the liver sections. Since bilirubins are processed in hepatocytes, they should be widely distributed within the cells. Combining SHG (green color) and 2PAF (red color) images, we found that the red autofluorescences of nontumor tissues mainly came from the granules within the hepatocytes (see Figure 6A–C). The distribution of

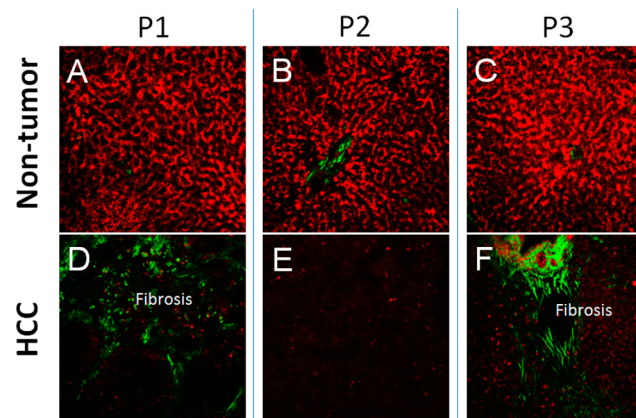


Figure 6. Combined 2PAF (red colors) and SHG (green) image set of nontumor (A–C) and poorly differentiated HCC (D–F) liver sections. Panels A and D, B and E, and C and F are pair sections from three patients (P1, P2, and P3). Their fields of view are $720 \mu\text{m} \times 720 \mu\text{m}$.

granules, in a large scale, showed typical pattern of sinusoids in livers. In contrast, for poorly differentiated HCC tissues, the bright granules disappeared and the average intensity of 2PAF was drastically decreased (Figure 6, parts D and F). Strong and widely spreading SHG signals indicate severed fibrosis in tissues (Figure 6, parts D and F). This reduction of red autofluorescence in HCC region was all observed in the three patients being investigated (Figure 6, parts A and D, B and E, and C and F). This microscopy evidence further supports the notion that the red 2PAF in livers originate from bilirubin dimers, which can serve as the optical contrast for the metabolic imaging of bilirubins in hepatocytes. In the future, we believe that medical doctors may even use this bilirubin metabolic imaging to define the boundaries of poorly differentiated HCC in surgery.

Using this unique contrast, we further investigated 19 different patients. For each section, we then took 2PAF images on three randomly selected regions with $720 \mu\text{m} \times 720 \mu\text{m}$ fields of view to obtain averaged 2PAF intensity per pixel. Upon

the integration of 2PAF intensities, we avoided the region with strong SHG since this portion is mostly occupied by collagens and not hepatocytes. The statistical results show that the 2PAF intensities of nontumor hepatocytes (37.1 ± 14.4 counts/pixel) were 1.6–10.7 times higher than those of their HCC counterparts (12.2 ± 5.7 counts/pixel) (Figure 7A). The

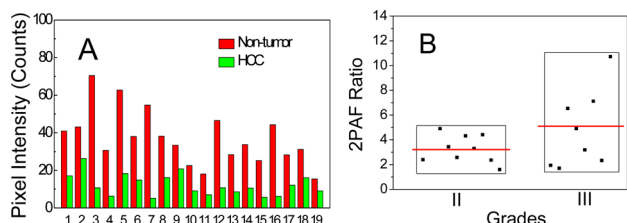


Figure 7. (A) Average 2PAF intensity of nontumor (red bars) and HCC (green bars) liver sections from 19 HCC patients. (B) The 2PAF ratio of nontumor part over HCC region grouped by its grading of histopathological reports.

average 2PAF contrast of nontumor part over HCC part was then calculated to be 3.7 times. In the paired *t* test analysis, the *t* value is 7.678 corresponding to $p \leq 0.001$, which indicates that the 2PAF of nontumor hepatocytes is significantly larger than that of poorly differentiated HCC regions. Grouped by its pathological grading, we found grade III patients on average have 4.8 ± 3.16 2PAF contrast, which is $\sim 50\%$ higher than that of grade II patients (contrast = 3.25 ± 1.2) (Figure 7B). This trend shows that higher grade and poorer-differentiated HCC tissues tend to have higher 2PAF contrast.

Fluorescence Lifetime Imaging Microscopy of HCC Tissues. Except for intensity, lifetime could be another dimension used for molecular imaging and even for diagnosis. Accordingly, we performed FLIM measurements on the liver sections from HCC patients. In this analysis, the lifetime trace of each pixel was also fitted by a two-exponential decay model, yielding *t*₁ and *t*₂ values (see the Materials and Methods section). For the nontumor part (Figure 8A), the histogram of fluorescence lifetime (Figure 8, parts C and D, solid curves) at each pixel peaked at [*t*₁ = 300 ps, *t*₂ = 1.5 ns], which was close to those of HSA-associated bilirubin dimers [*t*₁ = 240 ps, *t*₂ = 1.2 ns]. The difference of lifetimes may result from different molecular environment. For HCC sections, the signals were drastically reduced by 10-folds (Figure 8B, upper row). The extra 500 ps and 2 ns components emerged in the histogram (Figure 8, parts C and D, dotted curves), which could originate from the bilirubin dimers associated with other proteins. Such differences in lifetime histograms are a potential to be exploited as diagnosis indices to identify the HCC in liver tissues.

Metabolic Status versus Red Autofluorescence in Oral Cells. Harris and Werkhaven⁶¹ reported that protoporphyrin accumulation from malignant tumors was observed in ulcerated human oral carcinoma. Bilirubin is the downstream catabolite of protoporphyrin. Therefore, cancer cells may have different metabolic features on the 2PAF lifetimes of bilirubin dimers. Using the same optical system, we measured the FLIM of oral normal cells (SG) and cancer cell lines at precancer (DOK), carcinoma (SAS, OECM-1), and metastasis (HSC-3) stages (Figure 9, parts A and B). The histogram peak of lifetime *t*₁ and *t*₂ of SG cells was about 250 ps and 1.6 ns, respectively. All cancer cell lines showed longer distribution of *t*₁ and *t*₂ lifetimes (Figure 9C). The 30 cells statistics of histogram peaks for each cell line (Figure 9D) clearly indicates that cancer cell

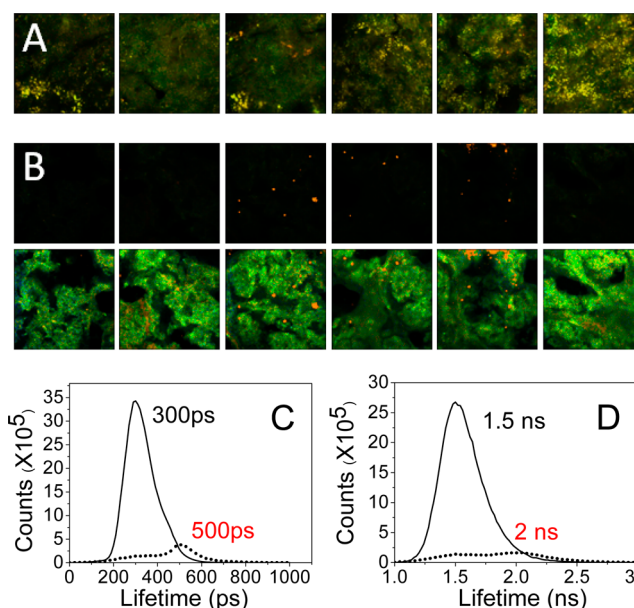


Figure 8. Fluorescence lifetime imaging microscopy of the *t*₁ component on cryosectioned liver tissues: (A) nontumor part and (B) poorly differentiated HCC. The image intensity of the lower column in panel B was enhanced up to 10-fold. (C) Lifetime histograms of *t*₁. (D) Lifetime histograms of *t*₂. The fields of view of FLIM images are $120 \mu\text{m} \times 120 \mu\text{m}$.

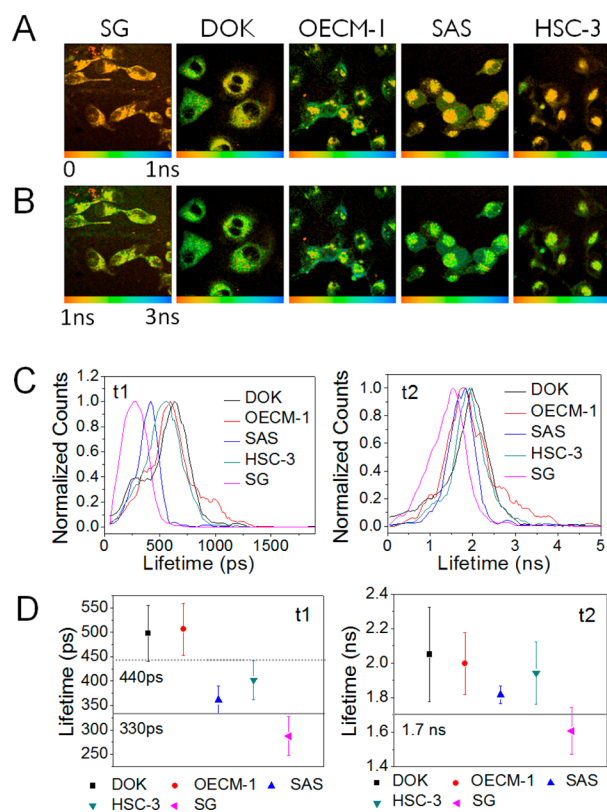


Figure 9. (A) *t*₁ and (B) *t*₂ fluorescence lifetime microscopy of oral normal cells (SG) and cancer cell lines at precancer (DOK), carcinoma (SAS, OECM-1), and metastasis (HSC-3) stages. (C) The lifetime histograms of *t*₁ and *t*₂. (D) The 30 cells statistics results of histogram peaks for each cell line.

lines exhibit emission lifetime *t*₁ longer than 330 ps (Figure 9D, left) and *t*₂ longer than 1.7 ns (Figure 9D, right). The OECM-1

1 and DOC cell lines even have t_1 times longer than 440 ps. These results indicate that the 2PAF lifetimes of bilirubin dimers could have the potential to diagnose cancers. Detailed biochemical mechanisms that cause such difference are worth further in-depth investigations.

CONCLUSION

In this study, we demonstrated for the first time that multiphoton excitation with a least-invasive femtosecond Cr:forsterite laser could make bilirubin dimers the dominant 2PAF contrast in biomedical tissues. Such a bilirubin imaging platform provides an opportunity for semiquantitative investigation of bilirubin metabolisms in living organisms with submicrometer spatial resolution. Efficient 2PAF of bilirubin dimers overwhelm the background autofluorescences from other endogenous molecules in cells. The specificity of molecular imaging was assured by the LC-MS measurement, fluorescence spectra, fluorescence lifetimes, and bile stains. Applying this combinational method on fresh liver sections, we found that poorly differentiated HCC would not uptake and process bilirubins. The absence of bilirubins drastically reduced the average 2PAF intensities of liver sections. Higher grades of HCC tend to result in higher 2PAF contrast between the nontumor part and the tumor site. This feature can be used to define the boundaries of poorly differentiated HCC and ensure whether there are residual tumor cells in the surgical resection of livers. Not just 2PAF intensities, we further found that the 2PAF lifetimes of intracellular bilirubin dimers can differentiate HCC from nontumor cells and oral cancer cells from normal oral cells. Oral cancer and HCC cells tend to have longer 2PAF lifetimes than nontumor ones. These findings validate that our platform of bilirubin metabolic imaging can be used as a semiquantitative tools to diagnose the disorder of bilirubin metabolisms in hepatobiliary diseases or cancers without extra staining.

ASSOCIATED CONTENT

Supporting Information

Additional information as noted in text. The Supporting Information is available free of charge on the ACS Publications website at DOI: 10.1021/acs.analchem.5b01903.

AUTHOR INFORMATION

Corresponding Authors

*E-mail: tmliu@ntu.edu.tw.

*E-mail: chop@ntu.edu.tw.

*E-mail: sun@ntu.edu.tw.

Author Contributions

Tzu-Ming Liu conceived the ideas, organized the experiments, made the measurements, and analyzed the data. Pi-Tai Chou provided help on chemical analysis. Chi-Kuang Sun supported the instrument and experimental environments.

Notes

The authors declare no competing financial interest.

ACKNOWLEDGMENTS

This study was funded by Ministry of Science and Technology, Taiwan under Grant Nos. NSC 98-2112-M-002-022, NSC 99-2628-E-002-009, and NSC 102-2221-E-002-195-MY3. This project was also funded by National Taiwan University under the program of Frontier and Innovation Research of National

Taiwan University, by the NTU Center of Genomic Medicines, and by the NTU Molecular Imaging Center.

REFERENCES

- (1) Watson, D.; Rogers, J. A. *J. Clin. Pathol.* **1961**, *14*, 271–8.
- (2) Rolinski, B.; Kuster, H.; Ugele, B.; Gruber, R.; Horn, K. *Clin. Chem.* **2001**, *47*, 1845–7.
- (3) Frei, B.; Stocker, R.; Ames, B. N. *Proc. Natl. Acad. Sci. U. S. A.* **1988**, *85*, 9748–52.
- (4) Vitek, L.; Schwertner, H. A. *Adv. Clin. Chem.* **2007**, *43*, 1–57.
- (5) Stocker, R.; Glazer, A. N.; Ames, B. N. *Proc. Natl. Acad. Sci. U. S. A.* **1987**, *84*, 5918–22.
- (6) Stocker, R.; Yamamoto, Y.; McDonagh, A. F.; Glazer, A. N.; Ames, B. N. *Science (Washington, DC, U. S.)* **1987**, *235*, 1043–6.
- (7) Belanger, S.; Lavoie, J. C.; Chessex, P. *Neonatology* **1997**, *71*, 233–8.
- (8) Gopinathan, V.; Miller, N. J.; Milner, A. D.; Rice-Evans, C. A. *FEBS Lett.* **1994**, *349*, 197–200.
- (9) Syapin, P. J. *Br. J. Pharmacol.* **2008**, *155*, 623–40.
- (10) Sarady-Andrews, J. K.; Liu, F.; Gallo, D.; Nakao, A.; Overhaus, M.; Ollinger, R.; Choi, A. M.; Otterbein, L. E. *Am. J. Physiol. Lung. Cell. Mol. Physiol.* **2005**, *289*, L1131–7.
- (11) Farombi, E. O.; Surh, Y. J. *J. Biochem. Mol. Biol.* **2006**, *39*, 479–91.
- (12) Sedlak, T. W.; Snyder, S. H. *Pediatrics* **2004**, *113*, 1776–82.
- (13) Tanaka, M.; Fukui, M.; Tomiyasu, K.; Akabame, S.; Nakano, K.; Hasegawa, G.; Oda, Y.; Nakamura, N. *Atherosclerosis* **2009**, *206*, 287–91.
- (14) Schwertner, H. A.; Vitek, L. *Atherosclerosis* **2008**, *198*, 1–11.
- (15) Vitek, L.; Ostrow, J. D. *Curr. Pharm. Des.* **2009**, *15*, 2869–83.
- (16) Lin, J. P.; Vitek, L.; Schwertner, H. A. *Clin. Chem.* **2010**, *56*, 1535–43.
- (17) Ndisang, J. F.; Lane, N.; Syed, N.; Jadhav, A. *Endocrinology* **2010**, *151*, 549–60.
- (18) Ndisang, J. F.; Jadhav, A. *Am. J. Physiol. Endocrinol. Metab.* **2009**, *296*, E829–41.
- (19) Dekker, D.; Dorresteijn, M. J.; Pijnenburg, M.; Heemskerk, S.; Rasing-Hoogveld, A.; Burger, D. M.; Wagener, F. A.; Smits, P. *Arterioscler., Thromb., Vasc. Biol.* **2011**, *31*, 458–63.
- (20) Bhuiyan, A. R.; Srinivasan, S. R.; Chen, W.; Sultana, A.; Berenson, G. S. *Metab., Clin. Exp.* **2008**, *57*, 612–6.
- (21) Choi, S. H.; Yun, K. E.; Choi, H. J. *Nutr., Metab. Cardiovasc. Dis.* **2013**, *23*, 31–7.
- (22) Kwon, K. M.; Kam, J. H.; Kim, M. Y.; Kim, M. Y.; Chung, C. H.; Kim, J. K.; Linton, J. A.; Eom, A.; Koh, S. B.; Kang, H. T. *J. Womens. He.* (2002) **2011**, *20*, 963–9.
- (23) Lin, L. Y.; Kuo, H. K.; Hwang, J. J.; Lai, L. P.; Chiang, F. T.; Tseng, C. D.; Lin, J. L. *Atherosclerosis* **2009**, *203*, 563–8.
- (24) Wu, Y.; Li, M.; Xu, M.; Bi, Y.; Li, X.; Chen, Y.; Ning, G.; Wang, W. *J. Diabetes* **2011**, *3*, 217–24.
- (25) Doumas, B. T.; Perry, B. W.; Sasse, E. A.; Straumfjord, J. V. *J. Clin. Chem.* **1973**, *19*, 984–93.
- (26) Bergmeyer, H. U. *Methods of Enzymatic Analysis*, 3rd ed.; VCH Verlagsgesellschaft GmbH: Weinheim, Germany, 1985.
- (27) Baranano, D. E.; Rao, M.; Ferris, C. D.; Snyder, S. H. *Proc. Natl. Acad. Sci. U. S. A.* **2002**, *99*, 16093–8.
- (28) Maghzal, G. J.; Leck, M. C.; Collinson, E.; Li, C.; Stocker, R. *J. Biol. Chem.* **2009**, *284*, 29251–9.
- (29) McDonagh, A. F. *Free Radical Biol. Med.* **2010**, *49*, 814–20.
- (30) Falchuk, K. H.; Contin, J. M.; Dziedzic, T. S.; Feng, Z.; French, T. C.; Heffron, G. J.; Montorzi, M. *Proc. Natl. Acad. Sci. U. S. A.* **2002**, *99*, 251–6.
- (31) Wang, J.; Luo, D. B.; Farias, P. A. M. *J. Electroanal. Chem. Interfacial Electrochem.* **1985**, *185*, 61–71.
- (32) Koch, T. R.; Akingbe, O. O. *Clin. Chem.* **1981**, *27*, 1295–9.
- (33) Palilis, L. P.; Calokerinos, A. C.; Grekas, N. *Anal. Chim. Acta* **1996**, *333*, 267–275.
- (34) Nath, N.; Chilkoti, A. *Anal. Chem.* **2004**, *76*, 5370–8.

- (35) Kurosaka, K.; Senba, S.; Tsubota, H.; Kondo, H. *Clin. Chim. Acta* **1998**, *269*, 125–36.
- (36) Shoham, B.; Migron, Y.; Riklin, A.; Willner, I.; Tartakovsky, B. *Biosens. Bioelectron.* **1995**, *10*, 341–352.
- (37) Fortuney, A.; Guilbault, G. G. *Electroanalysis* **1996**, *8*, 229–232.
- (38) Klemm, J.; Prodromidis, M. I.; Karayannis, M. I. *Electroanalysis* **2000**, *12*, 292–295.
- (39) Huang, C. Y.; Syu, M. J.; Chang, Y. S.; Chang, C. H.; Chou, T. C.; Liu, B. D. *Biosens. Bioelectron.* **2007**, *22*, 1694–9.
- (40) Syu, M. J.; Chiu, T. C.; Lai, C. Y.; Chang, Y. S. *Biosens. Bioelectron.* **2006**, *22*, 550–7.
- (41) Rahman, M. A.; Lee, K. S.; Park, D. S.; Won, M. S.; Shim, Y. B. *Biosens. Bioelectron.* **2008**, *23*, 857–64.
- (42) Wang, C.; Wang, G.; Fang, B. *Microchim. Acta* **2009**, *164*, 113–118.
- (43) Lee, K. S.; Gartner, L. M. *Pediatr. Res.* **1976**, *10*, 782–788.
- (44) Rosei, M. A. *Experientia* **1983**, *39*, 165–6.
- (45) Glushko, V.; Thaler, M.; Ros, M. *Biochim. Biophys. Acta* **1982**, *719*, 65–73.
- (46) Liu, T. M.; Hsieh, C. T.; Chen, Y. S.; Huang, F. L.; Huang, H. Y.; Lee, W. J.; Kung, C. T.; Sun, C. K. *Proc. of SPIE* **2011**, *7903*, 79032Z ·1–6.
- (47) Wong, D. Y.; Chang, K. W.; Chen, C. F.; Chang, R. C. J. *Oral Maxillofac. Surg.* **1990**, *48*, 385–390.
- (48) Yang, S. C.; Lin, S. C.; Chiang, W. F.; Yen, C. Y.; Lin, C. H.; Liu, S. Y. *J. Oral Pathol. Med.* **2003**, *32*, 600–605.
- (49) Braslavsky, S. E.; Holzwarth, A. R.; Schaffner, K. *Angew. Chem., Int. Ed. Engl.* **1983**, *22*, 656–674.
- (50) Skala, M. C.; Riching, K. M.; Gendron-Fitzpatrick, A.; Eickhoff, J.; Eliceiri, K. W.; White, J. G.; Ramanujam, N. *Proc. Natl. Acad. Sci. U. S. A.* **2007**, *104*, 19494–9.
- (51) Wagner, J. R.; Brunzelle, J. S.; Forest, K. T.; Vierstra, R. D. *Nature* **2005**, *438*, 325–31.
- (52) Kohashi, K.; Date, Y.; Morita, M.; Tsuruta, Y. *Anal. Chim. Acta* **1998**, *365*, 177–182.
- (53) Huang, C.-C.; Chuang, K.-Y.; Huang, C.-J.; Liu, T.-M.; Yeh, C.-S. *J. Phys. Chem. C* **2011**, *115*, 9952–9960.
- (54) Ostrow, J. D.; Mukerjee, P.; Tiribelli, C. J. *Lipid Res.* **1994**, *35*, 1715–1737.
- (55) Brodersen, R. *Acta Chem. Scand.* **1966**, *20*, 2895–2896.
- (56) Pu, Y.-M.; Lightner, D. A. *Spectrosc. Lett.* **1991**, *24*, 983–993.
- (57) Carey, M. C.; Koretsky, A. P. *Biochem. J.* **1979**, *179*, 675–689.
- (58) Lightner, D. A.; Trull, F. R. *Spectrosc. Lett.* **1983**, *16*, 785–803.
- (59) Boiadjiev, S. E.; Watters, K.; Wolf, S.; Lai, B. N.; Welch, W. H.; McDonagh, A. F.; Lightner, D. A. *Biochemistry* **2004**, *43*, 15617–15632.
- (60) Beaven, G. H.; Anne d'ALBIS; Walter, B. G. *Eur. J. Biochem.* **1973**, *33*, 500–510.
- (61) Harris, D. M.; Werkhaven, J. *Lasers Surg. Med.* **1987**, *7*, 467–72.